

A linear assessment of barotropic Rossby wave propagation in different background flow configurations

Antonio Segalini¹, Jacopo Riboldi¹, Volkmar Wirth², and Gabriele Messori^{1,3,4,5}

¹Department of Earth Sciences, Uppsala University, Villavägen 16, 752 36 Uppsala, Sweden

²Institute for Atmospheric Physics, Johannes Gutenberg University Mainz, Becherweg 21, 55128 Mainz, Germany

³Centre of Natural Hazards and Disaster Science (CNDS), Uppsala University, Villavägen 16, 75236 Uppsala, Sweden

⁴Department of Meteorology, Stockholm University, Svante Arrhenius väg 16c, 114 18 Stockholm, Sweden

⁵Bolin Centre for Climate Research, Stockholm University, Svante Arrhenius väg 8, 114 18 Stockholm, Sweden

Correspondence: Antonio Segalini (antonio.segalini@geo.uu.se)

Abstract. The horizontal propagation of Rossby waves in the upper troposphere has been a long-standing topic in dynamical meteorology for a number of reasons. More recently, it has been suggested that the concept of “waveguidability” may be useful in this context. With an eye to such issues, the current paper suggests a novel and efficient algorithm to solve the linearized barotropic vorticity equation on the sphere in a forced-dissipative configuration. The algorithm allows one to obtain linear wave solutions resulting from arbitrary combinations of the forcing and the background zonal wind. Examples using single- and double-jet configurations illustrate that the proposed solutions allow one to quantify to what extent the background flow acts as a zonal waveguide for Rossby waves. The onset of barotropic instability might hinder the applicability of the linear framework, but it is shown that the nonlinear flow evolution can still be retrieved qualitatively from the linearized solution both for the stationary component of the wave field and for the evolution of transient waves.

10 1 Introduction

Rossby waves are a fundamental component of the upper-tropospheric dynamics (Rossby, 1939, 1940) and are instrumental in modulating the location, intensity, and track of extratropical weather systems. They can be forced by baroclinic instability, large-scale topographical features, and meso- to large-scale diabatic heating (e.g., Rhines, 1975; Hoskins and Karoly, 1981; Held, 1983; Garcia and Salby, 1987; Held et al., 2002; Brayshaw et al., 2009; Garfinkel et al., 2020; Martius et al., 2021). A key characteristic of Rossby waves, which has profound implications for their modulation of weather systems, is their propagation. The Earth’s spherical geometry usually leads to the equatorward refraction of Rossby waves (Hoskins and Karoly, 1981), yet the presence of localised upper tropospheric jet streams can favour a zonal propagation (e.g., Hoskins and Valdes, 1990; Ambrizzi et al., 1995; Branstator, 2002; Wirth et al., 2018). The capability of jet streams to promote Rossby wave propagation, referred to as “waveguidability”, has long been object of research (see the reviews by Wirth et al., 2018; White et al., 2022). Waveguides typically exist for time scales longer than the waves they “guide”, and this property can be exploited to understand persistence and predictability of midlatitude weather (Martius et al., 2010).

The amplification and propagation of Rossby waves along such waveguides has been related in the literature to the occurrence of extreme weather events both in winter (e.g., Davies, 2015; Harnik et al., 2016) and summer (e.g., Kornhuber et al., 2019; Teng and Branstator, 2019; Di Capua et al., 2021; Rousi et al., 2022; Jiménez-Esteve et al., 2022). In a number of these
25 examples, Rossby waves were identified as quasi-stationary and associated with concurrent extremes in geographically remote regions due to the zonally-extended, large-amplitude nature of the waves. The existence of quasi-stationary waves on a mid-latitude waveguide has also been linked to the phenomenon of quasi-resonance, namely a constructive self-interference of the wave, which in turn may be linked to surface extreme events (Petoukhov et al., 2013; Coumou et al., 2014); however, whether or not quasi-resonance is a relevant mechanism in realistic situations is an unsolved question (Wirth and Polster, 2021). In
30 a longer term perspective, anthropogenic global warming can modify the position and strength of extratropical waveguides, thus systematically affecting the amplitude and the propagation of Rossby waves and the persistence of the associated weather systems (Hoskins and Woollings, 2015).

The relevance that waveguidability plays in atmospheric dynamics, as well as its connection to surface extremes in a changing climate, has led to a renewed interest in its study (White et al., 2022). In general, waveguidability is regarded as a property
35 of the background flow configuration in which Rossby waves are propagating. The concept of background flow is useful for decomposing the atmospheric flow into a background component that varies gradually in space and time, and a wave component (i.e., the Rossby waves in the present work) that varies more rapidly. The feasibility of such a decomposition inherently relies on the assumption that a clear scale separation exists between the waves and the background flow, such that the former are not leaving an immediate signature on the latter. The identification of the background flow can be practically done by using
40 time and/or zonal averages, a methodology based on the assumed linearity of the waves: However, this assumption is violated when Rossby waves reach significant meridional amplitudes, as often happens in the context of large-scale flow configurations associated with unusual or extreme weather (Wirth and Polster, 2021).

The role of specific background flow configurations in promoting waveguidability can be investigated in detail using idealized frameworks. Manola et al. (2013) and Wirth (2020) are notable examples of such work for the cases of single, localized
45 jet streams in the Northern Hemisphere. These studies noticed that waveguidability increases with the strength of the jet and that latitudinally narrow jets are more efficient waveguides than broad jets. Steady wave patterns have been discussed by means of the ray-tracing technique (Hoskins and Karoly, 1981; Hoskins and Ambrizzi, 1993; Wirth, 2020) where the β -plane analysis of Rossby waves is extended to slowly meridionally-varying background flows by means of WKB theory and a Mercator projection. This enabled to identify waveguides as ridges in the so-called refractive index, drastically simplifying the problem
50 with respect to a full eigenvalue analysis. However, the ray-tracing approach is subject to some crucial limitations. It is often implemented on a Mercator projection of the flow field, leading to distortion in the high latitudes, and the meridional/longitudinal variation of the background flow must be gradual compared to the scale of the wave. Moreover, although ray-tracing can in principle be applied to transient waves, in practice it is typically used for the study of stationary waves (with the notable exception of Yang and Hoskins, 1996). One therefore loses information about how the waves are evolving in time or whether
55 the flow will ever approach a steady state. A critical assessment of this approach was performed by Wirth (2020), albeit limited to only a few background flows. There is indeed a lack of understanding of Rossby waveguides in complex background flow

configurations, such as the presence of two separate jet streams, which has been linked to summertime heatwaves (“double jets”; e.g., Coumou et al., 2014; Rousi et al., 2022). **Understanding waveguidability thus requires** a systematic investigation of a large number of different background flows. Each case must also be investigated for different forcings to assess the flow response, and this task becomes quickly demanding in terms of computational resources and expert analysis time.

Motivated by this open challenge and by the limitations of ray-tracing theory, we extend in this paper the framework of Wirth (2020) to study the propagation of forced Rossby waves without recourse to ray-tracing and avoiding numerical integration of the underlying nonlinear equations. Similar approaches have been previously employed to study other types of oscillatory phenomena, such as Rossby wave critical layers (Campbell and Maslowe, 1998), equatorial waves (Boyd, 1978) and gravity waves (Baldauf and Brdar, 2013). Specifically, we study **Rossby waves evolution** by solving explicitly the linearized, 2-D barotropic vorticity equation in terms of normal mode analysis. This enables one to inexpensively obtain solutions for any forcing under a given zonally symmetric background flow; furthermore, it allows one to study **Rossby wave propagation without the limitations imposed by ray-tracing methods, such as the assumption of scale-separation or the need to project the flow on a Mercator plane.** We first validate the solutions by comparing them with the output of nonlinear numerical simulations based on a spectral code built on spherical harmonics. The joint analysis of linear and nonlinear solutions further allows a detailed investigation of the stability of different wave modes, **providing information about the transient evolution of the Rossby waves.** In the end we use the novel algorithm in order to extend the analysis of waveguidability of idealized zonal jets beyond what has been done in previous publications. The paper is structured as follows: Section 2 presents the theory behind the linear approach, while its discrete implementation based on orthogonal Chebyshev polynomials is discussed in the paper appendix. A comparison between linear and nonlinear calculations is discussed in section 3 where different zonal wind profiles are investigated in terms of both the wave spatial structure and of integrated parameters such as the waveguidability. **The stationary solutions for single-jet and double-jet configurations are discussed respectively in sections 4 and 5. Time-dependent solutions are presented in Sect. 6. The paper is closed by some concluding remarks in section 7.**

2 Model framework and numerical details

Let us consider the two-dimensional barotropic vorticity equation on a spherical planet with radius a^* (in this section dimensional quantities are indicated by means of an asterisk superscript)

$$\frac{\partial \zeta^*}{\partial t^*} + (\mathbf{V}^* \cdot \nabla_h)(\zeta^* + f^*) = -\chi^* (\zeta^* - \bar{\zeta}^*) + F^*, \quad (1)$$

where \mathbf{V}^* is the horizontal velocity field, $f^* = 2\Omega^* \cos \theta$ is the Coriolis parameter, $\theta = \pi/2 - \varphi$ is the colatitude (associated with the latitude φ) and λ is the longitude. **Similarly to Hoskins and Ambrizzi (1993) and Wirth (2020),** a damping term $-\chi^* (\zeta^* - \bar{\zeta}^*)$ is present: this term provides a stabilizing effect that hinders a too strong departure of the atmospheric state from the background vorticity. **F^* indicates a generic forcing in space and time. By normalizing** physical quantities with respect to the planetary radius a^* and a characteristic velocity U_s^* such that

$$t = \frac{t^*}{a^*/U_s^*}, \quad \mathbf{V} = \frac{\mathbf{V}^*}{U_s^*}, \quad \zeta = \frac{\zeta^*}{U_s^*/a^*}, \quad f = \frac{f^*}{2\Omega^*} = \cos \theta, \quad F = \frac{F^*}{(U_s^*/a^*)^2}, \quad (2)$$

the barotropic vorticity equation (1) is re-written in dimensionless form as

$$90 \quad \frac{\partial \zeta}{\partial t} + (\mathbf{V} \cdot \nabla_h) \left(\zeta + \frac{f}{\text{Ro}} \right) = -\chi (\zeta - \bar{\zeta}) + F \quad \text{with} \quad \text{Ro} = \frac{U_s^*}{2\Omega^* a^*}. \quad (3)$$

The choice of the characteristic velocity scale, U_s^* , is arbitrary but it should be of the same order of magnitude of the velocity field. In the considered two-dimensional case, the flow divergence is zero everywhere so that a streamfunction, Ψ , can be introduced, facilitating the determination of the velocity and vorticity fields as

$$u_\theta = -\frac{1}{\sin \theta} \frac{\partial \Psi}{\partial \lambda}, \quad u_\lambda = \frac{\partial \Psi}{\partial \theta}, \quad \zeta = \nabla^2 \Psi. \quad (4)$$

95 By assuming a base zonal flow $u_\lambda = U(\theta)$ and $u_\theta = 0$, the undisturbed vorticity, $\bar{\zeta}$, is given by

$$\bar{\zeta}(\theta) = \frac{1}{\sin \theta} \frac{\partial}{\partial \theta} (U \sin \theta) = \cot \theta U + \frac{\partial U}{\partial \theta} \quad \text{for} \quad 0 < \theta < \pi. \quad (5)$$

Let us consider a perturbed problem where the relative vorticity is given by $\zeta = \bar{\zeta} + \zeta'$. This will be associated with a streamfunction, $\bar{\Psi} + \psi'$, and velocity field

$$\mathbf{V} = (u_\theta, u_\lambda) = (0, U) + (u'_\theta, u'_\lambda) = (0, U) + \left(-\frac{1}{\sin \theta} \frac{\partial \psi'}{\partial \lambda}, \frac{\partial \psi'}{\partial \theta} \right). \quad (6)$$

100 The equation governing the small perturbation is obtained by taking (3) and subtracting the base-state equation. By neglecting the nonlinear terms, one obtains the linearised barotropic vorticity equation

$$\frac{\partial \zeta'}{\partial t} + \frac{U}{\sin \theta} \frac{\partial \zeta'}{\partial \lambda} + u'_\theta \frac{\partial}{\partial \theta} \left(\bar{\zeta} + \frac{f}{\text{Ro}} \right) = -\chi \zeta' + F, \quad (7)$$

with

$$\zeta' = \nabla_h^2 \psi' \quad , \quad u'_\theta = -\frac{1}{\sin \theta} \frac{\partial \psi'}{\partial \lambda}. \quad (8)$$

105 The system can be better analysed by taking the Fourier transform in the zonal direction (with wavenumber m) leading to

$$\frac{\partial \hat{\zeta}}{\partial t} + \left(\frac{imU}{\sin \theta} + \chi \right) \hat{\zeta} + \hat{u}_\theta \frac{\partial}{\partial \theta} \left(\bar{\zeta} + \frac{f}{\text{Ro}} \right) = \hat{F}, \quad (9)$$

where

$$\hat{\zeta} = \frac{\partial^2 \hat{\psi}}{\partial \theta^2} + \cot \theta \frac{\partial \hat{\psi}}{\partial \theta} - \frac{m^2}{\sin^2 \theta} \hat{\psi} = \mathcal{L} \hat{\psi} \quad , \quad \hat{u}_\theta = -\frac{im}{\sin \theta} \hat{\psi}, \quad (10)$$

and \mathcal{L} indicates the Laplace operator that, once discretised, becomes a matrix. By introducing the matrix $B = i\mathcal{L}$ and the streamfunction vector $\hat{\psi}_j = \hat{\psi}(\theta_j; m)$ evaluated at the colatitudes θ_j , the barotropic vorticity equation (9) is written as

$$-iB \frac{\partial \hat{\psi}_j}{\partial t} + \left[\left(\frac{imU}{\sin \theta} + \chi \right) \mathcal{L} - \frac{im}{\sin \theta} \frac{\partial}{\partial \theta} \left(\bar{\zeta} + \frac{f}{\text{Ro}} \right) I \right] \hat{\psi}_j = -iB \frac{\partial \hat{\psi}_j}{\partial t} + A \hat{\psi}_j = \hat{F}, \quad (11)$$

where the terms composing the matrix A are grouped within the square brackets in (11) and I is the identity matrix (see appendix A for a detailed description of how the differential operators are discretized and the matrices are constructed). Equation

(11) is a linear system of ordinary differential equations in time with the streamfunction at the collocation points as unknowns.

115 By erasing the time derivative, the equilibrium state of the linearised system is obtained as

$$\widehat{\psi}_j = A^{-1}\widehat{F}, \quad (12)$$

similar to the formula provided by Hoskins and Karoly (1981). Eq.(12) corresponds to the steady solution of the forced dynamical system achieved at regime if the system is stable (see discussion below for the flow stability analysis). Even if the system is unstable, the state described by Eq. (12) is the only one that erases the time derivative of the linearised system: thus, we choose to name it “equilibrium solution”. Its determination is only related to the advection and dissipation of vorticity rather than the vorticity temporal evolution and can therefore be obtained in one computational step.

120

The solution of Eq.(11) describing the growth of an infinitesimally small perturbation (be it initiated by the forcing or by a generic initial condition) can be written as the sum of the homogeneous solution (starting from a given initial condition) plus a forced solution. By introducing a perturbation as a modal ansatz $\widehat{\psi}_j = \overline{\psi}_j e^{-i\omega t}$ it is possible to solve the homogeneous problem as an eigenvalue one, identifying the complex eigenvalues, ω , and the associated eigenfunctions for each azimuthal wavenumber, m . The advantage of the proposed framework is that the behaviour of the system is determined from the eigenvalues of the homogeneous problem, that are *independent* of the forcing and have indeed general validity for a given zonal background flow. If all the complex eigenvalues have negative imaginary part the system is stable and it will converge to the equilibrium state given by Eq. (12), while the perturbations will grow with time if at least one eigenvalue has positive imaginary part. Thus, the sign of the imaginary part of the eigenvalues determines whether a perturbation will grow or decay. The real part of the eigenvalues, on the other hand, is associated with phase propagation in the zonal direction. In this framework, the evolution of the perturbation is obtained as an initial value problem, drastically simplified by means of the modal analysis (details are provided in the Appendix).

130

3 Model setup and validation

135

The proposed linearized framework, based on Chebyshev polynomials for the treatment of the solution in the meridional direction (from now on referred to as the linear method), is first compared with the test cases proposed by Wirth (2020) for two of the investigated zonal velocity profiles. The code has been written in Python, where Chebyshev polynomials have been implemented following Peyret (2002) and Canuto et al. (2006). In all simulations, only the dissipative term $-\chi^* \nabla_h^2 \psi'$ (with $\chi^* = (7 \text{ d})^{-1}$ as in Wirth, 2020) was used to make the barotropic wave decay and no hyperviscosity was introduced. The planetary radius was taken as 6371 km while the planetary rotation speed was $\Omega = 7.292115 \cdot 10^{-5} \text{ rad s}^{-1}$.

140

The linear problem has been discretized into an equal number of latitudes and longitudes without any aliasing consideration or numerical stability constraints. In order to check the code correctness, an independent numerical solution of the barotropic vorticity equation has been implemented by using the spherical harmonics transform (SHT) package from Schaeffer (2013). Both the linear and nonlinear barotropic vorticity equations were implemented and compared to the results of the proposed linearised framework. A triangular truncation scheme was adopted with an aliasing-removal approach in both the linear and

145

nonlinear simulation with spherical harmonics (although this **made a difference only for the nonlinear simulations**). A leapfrog scheme was used for the temporal discretization with a time step of 10 minutes. A Robert-Asselin filter with filter parameter 0.01 was implemented to eliminate the spurious computational mode associated with the leapfrog method (Kalnay, 2003).

Since the topographic forcing F is stationary, the constant forcing solution provided by Eq. (A7) is used. The expression
 150 is further simplified here as the initial perturbation streamfunction is assumed to be zero, implying the vanishing of the first term of Eq. (A7), so that only the forced response needs to be computed. **The forced response is obtained from the method of variation of constants and therefore facilitated by the eigenfunctions calculated from the homogeneous problem**

In the special case of solid body zonal velocity profile, $U = \bar{U} \sin \theta = \bar{U} \cos \varphi$, **the zonal velocity is obtained as if the atmosphere was rotating at a slightly higher angular velocity than Ω** and the linearised homogeneous barotropic vorticity
 155 equation (7) reduces to

$$\frac{\partial \nabla_h^2 \psi'}{\partial t} + \bar{U} \frac{\partial \nabla_h^2 \psi'}{\partial \lambda} + 2(\bar{U} + \Omega a) \frac{\partial \psi'}{\partial \lambda} + \chi \nabla_h^2 \psi' = 0. \quad (13)$$

Equation (13) can be solved analytically by means of the ansatz $\psi' \propto Y_l^m(\theta, \lambda) e^{-i\omega t}$ where Y_l^m is the spherical harmonic with degree l and order m . The resulting dispersion relationship is

$$\omega = m \left[\bar{U} - \frac{2\bar{U} + 2\Omega a}{l(1+l)} \right] - i\chi, \quad (14)$$

160 which is a well-known analytical result for Rossby-Haurwitz waves (Haurwitz, 1940). The attenuation parameter χ makes the eigenvalue stable, while the first term of Eq. (14) is associated with the zonal phase propagation of the wave, similarly to the planar case. From this analysis it is already known that all the modes of the solid-body zonal velocity case are stable (since $\chi > 0$), that the modes are spherical harmonics and that the dispersion relationship is given by Eq. (14). Simulations done with different grid resolutions showed an excellent agreement between the analytical relationship (14) and the numerical
 165 eigenvalues, with error comparable to the precision of the machine (not shown).

Fig. 1a shows the meridional velocity field (positive northward) and the associated wave pattern at the equilibrium state (12) created by a smooth, idealized mountain located at latitude $\varphi_F = 45^\circ\text{N}$ and longitude $\lambda_F = 30^\circ\text{E}$ and described by

$$F = -7.73 \cdot 10^{-9} (\lambda - \lambda_F) \exp \left[-\frac{(\varphi - \varphi_F)^2}{2\sigma_{\varphi,F}^2} - \frac{(\lambda - \lambda_F)^2}{2\sigma_{\lambda,F}^2} \right] h_F, \quad (15)$$

where $\sigma_{\varphi,F} = \sigma_{\lambda,F} = 10^\circ$ and $h_F = 0.3$, unless otherwise stated. The zonal background flow is given by $U = 15 \cos \varphi \text{ m s}^{-1}$
 170 (or with $\bar{U} = 15 \text{ m s}^{-1}$ as above). Fig. 1a should be compared to the nonlinear solution in Fig. 3a of Wirth (2020): The structure of the wave pattern is very similar, although here obtained without any time integration since the flow will in time **approach** the steady-state solution because the imaginary part of the eigenvalues is negative. The linear spherical harmonics solution is practically identical to the Chebyshev approach and therefore the results will not be shown here. The nonlinear solver has slight differences from the linear method, such as a more rapid wave attenuation away from the forcing (as visible in Fig. 1b).

175 A sensitivity study can be performed for different grid resolutions **to assess the appropriate number of polynomials to be used in order to achieve a desired convergence**. The waveguidability, calculated as defined in Wirth (2020), has been used here

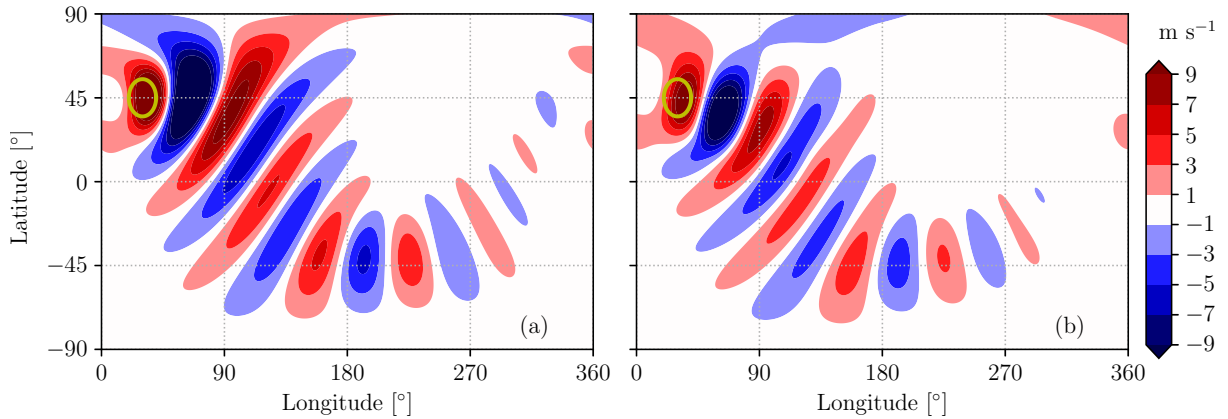


Figure 1. Meridional velocity pattern at the equilibrium state for the zonal velocity profile $U = 15 \cos \varphi$ from the linear analysis (a) and after 100 days with the nonlinear solver (b). The circle indicates the topographic forcing.

as the key quantity for the comparison. The estimate by Wirth (2020) corresponds to the ratio between the enstrophy found in a monitoring region downstream of the forcing (180°E and 270°E, 30°N and 60°N) and the total enstrophy integrated over all latitudes across 180°E and 270°E. Fig. 2a shows the convergence of the waveguidability around 45°N for different grid resolutions in order to quantify the minimum number of polynomials needed for numerical convergence. It is noteworthy that the convergence of the results is obtained even for moderate resolutions with the linear Chebyshev and linear SHT methods, while the nonlinear method approaches a lower value of waveguidability, suggesting a difference between linear and nonlinear analyses. Having assessed the grid convergence, the rest of the work will use grid resolution $N = 256$ for the solution of the linearized eigenvalue problem via Chebyshev polynomials while a T170 truncation will be used for the nonlinear spherical harmonics simulations.

With this setup, we notice that the linear method is capable of replicating the waveguidability increase with jet speed, obtaining similar values of the metric employed by Wirth (2020) for a jet located at 45°N (Fig. 2b). The difference between the linear and nonlinear solutions must be related to a dissipative effect of the nonlinear terms, neglected in the linear analysis. The above waveguidability metric, however, cannot be easily applied to compare waveguides located at different latitudes: in fact, the physical distance between the forcing and the monitoring sector would vary when the jet latitude is changed, leading to a spurious increase of waveguidability towards the Pole. An adapted metric will be proposed in Sec. 4.1 in the attempt to provide a definition able to account for jets at different latitudes.

4 Single-jet configurations

We will now focus on the case of a latitudinally-confined jet, using the formulation by Wirth (2020)

$$U = \bar{U} \cos \varphi + U_J \exp \left[-\frac{(\varphi - \varphi_J)^2}{2\sigma_J^2} \right] + L(\varphi), \quad (16)$$

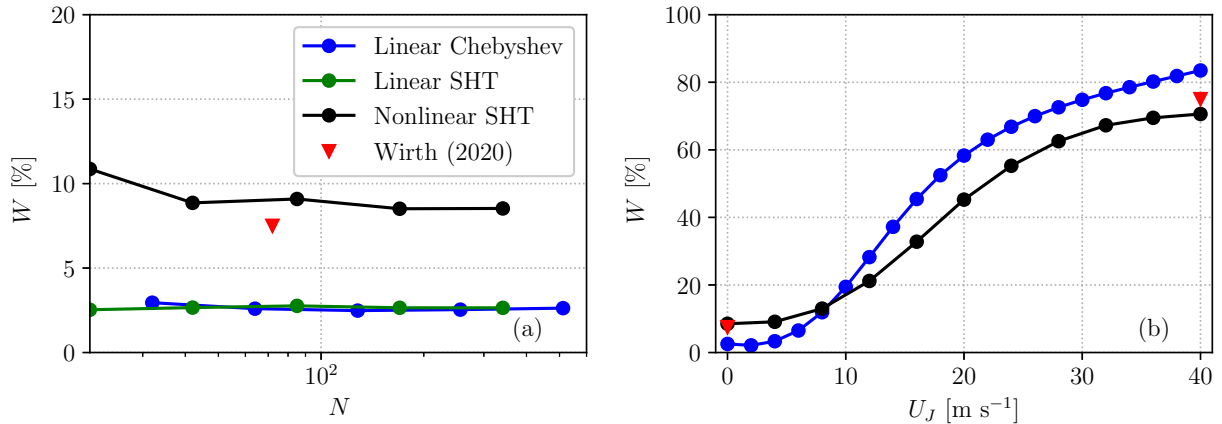


Figure 2. (a) Waveguidability for a Gaussian mountain located at $\varphi_F = 45^\circ\text{N}$ estimated from different linear and nonlinear simulations at different grid resolutions when $U = 15 \cos \varphi \text{ m s}^{-1}$ (namely without any latitudinally-confined jet). N for the Chebyshev simulations is given by the number of latitude/longitudes grid points, while for the simulations with the SHT method it is given by the truncation number. (b) Waveguidability assessed for the linear and nonlinear simulations for $N = 256$ (corresponding to a T170 resolution) for different jet velocities U_J (according to the zonal velocity profile given in Eq. 16).

where U_J is the jet velocity, $\bar{U} = 15 \text{ m s}^{-1}$, $\varphi_J = 45^\circ\text{N}$ is the jet latitude and $\sigma_J = 5^\circ$ (unless otherwise stated). L indicates a linear correction that imposes $U = 0$ at the two poles.

4.1 Waveguidability assessment

200 Determining a universal estimate of waveguidability is still an open question: Waveguidability should inform about the ability of waveguides to duct waviness and should be in principle applicable to any background flow. While developing a universal waveguidability metric is not the focus of the current study, we nonetheless need a metric that enables comparison of back-ground flows with jets at different latitudes. Here, we opt to consider the amount of enstrophy that remains at the forcing latitude compared to the total one. This implies a minimal change with respect to Wirth (2020), with an integration over all longitudes rather than just a sector. The normalized meridional enstrophy density E of a jet centered around $\varphi = \varphi_0$ is here
 205 defined as

$$E(U_J, \varphi_0) = \frac{\int_{\varphi_0 - \Delta\varphi}^{\varphi_0 + \Delta\varphi} \cos \varphi \int_0^{2\pi} \mathcal{E}(\varphi, \lambda) d\lambda d\varphi}{\int_{-\pi/2}^{\pi/2} \cos \varphi \int_0^{2\pi} \mathcal{E}(\varphi, \lambda) d\lambda d\varphi}, \quad (17)$$

where $\Delta\varphi = 15^\circ$ and $\mathcal{E}(\varphi, \lambda) = \overline{(\zeta - \zeta_0)^2} / 2$ is the enstrophy of the 90 days time averaged vorticity anomaly from the back-ground state (if a temporal steady state is achieved, the time averaging is unnecessary and only the final time is considered). It is important to consider that this definition requires a forcing centered around φ_0 as a source of vorticity. The so-defined
 210 normalized meridional enstrophy density takes into account the enstrophy in the vicinity of the forcing, which will be high even in absence of jet streams and thus cannot be directly used as a measure of the waveguidability.

With the help of the newly developed linear method, it is possible to very efficiently estimate the equilibrium state for many jet velocities and jet latitudes and use it to calculate E . This is shown in Fig. 3a for single jets with different jet latitudes and strengths. It is clear that the stronger the jet, the higher the normalized enstrophy density E , as noticed already for the jet at 45°N. However, when no jet is present (and therefore no waveguide should exist) E remains still high due to the enstrophy generated in the vicinity of the forcing. We also notice that E increases with latitude, as more enstrophy is found along the short latitude circles close to the Pole.

In order to isolate just the contribution of the waveguide in keeping the energy at that latitude, Fig. 3b shows the difference ΔE between $E(U_J, \varphi_0)$ and $E(0, \varphi_0)$ (namely the normalized enstrophy density without any jet assessed at that latitude). Removing the contribution of solid-body rotation isolates the increase in E due to the presence of a waveguide. We see that ΔE increases with jet speed in a consistent way for all latitudes. An equatorial westerly jet (which is obviously not relevant to realistic situations) results in a weaker ΔE than in midlatitudes; this last result is presumably due to the fact that the Equator already constitutes a waveguide for a background solid body rotation even without any jet superimposed.

The increment ΔE due to the presence of the jet is, as expected, small for low jet speeds. However, even for the high jet speed of 40 m s⁻¹ ΔE remains below 50% suggesting that ΔE is not an appropriate measure of waveguidability for strong jets. In order to propose a simple assessment of the waveguidability property, one could consider how ΔE compares to an “ideal” waveguide at the same latitude, i.e., a waveguide that would keep all the enstrophy in the same latitude circle of the jet ($E = 1$). This could be computed as the ratio

$$W(U_J, \varphi_0) = \frac{E(U_J, \varphi_0) - E(0, \varphi_0)}{1 - E(0, \varphi_0)}, \quad (18)$$

that is defined to be a number between 0 (no jet) and 1 (ideal waveguide). This ratio gives a direct measure of how the normalized enstrophy density is increased by the jet presence, relative to the increase achievable with an ideal waveguide. The so-defined waveguidability increases with jet speed from 0 to around 90%, as expected, but it also features an increase with latitude for strong jets (Fig. 3c). This trend of W with latitude is likely not due to the fact that high-latitude jets act as better waveguides than low-latitude jets, because ΔE (i.e., the numerator of W) does not feature an analogous latitudinal variation. On the other hand, it likely results from the relative variation of $E(0, \varphi_0)$ with latitude visible in Fig. 3a, which leads to a reduction of the denominator of Eq. (18) at high latitudes. From a physical point of view, this means that a large part of the enstrophy is already kept at the latitude of the forcing even in the absence of a jet: For this reason, it is much easier to approach the status of “ideal waveguide” at high latitudes than at low latitudes, at least according to our metric. The presence of resonance at high latitudes is also not be ruled out, but its assessment would require a more targeted investigation.

The issues outlined above make us acknowledge that the proposed definition of waveguidability is also “neither universal nor exact” (Wirth, 2020). Equation (18) is indeed a pragmatic expression developed for single jets, considering the background flow associated with solid-body rotation as the reference state used in both the numerator and denominator of W . This choice is well-suited for background flows with a single jet. Later in this study we also apply it to a double-jet case, although we recognize that a more general approach should be developed for that and other more complex background flows.

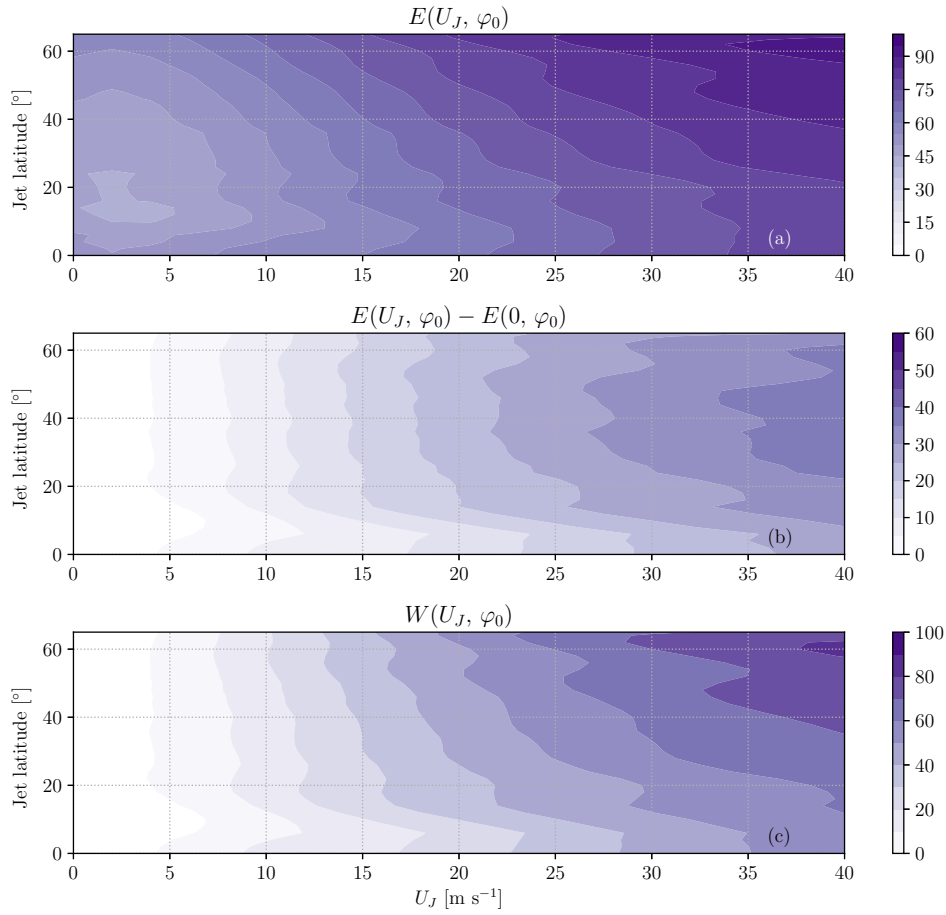


Figure 3. (a) Normalized meridional entrophy density of the single jet zonal profiles (as in Eq. 16) for different jet latitudes and strengths, estimated according to Eq. (17) with φ_0 equal to the jet latitude. The entrophy field has been computed from the equilibrium state obtained from Eq. (12), namely from the linear method. Only narrow jets with $\sigma_J = 5^\circ$ have been considered. (b) Difference $E(U_J, \varphi_0) - E(0, \varphi_0)$ used to highlight the increment in normalized entrophy density with the jet speed with respect to the solid-body case. (c) Estimated waveguidability calculated according to Eq. (18).

245 4.2 The strong-jet case

The strong-jet case with $U_J = 40 \text{ m s}^{-1}$, associated with the highest waveguidability, is characterized by an unsteady velocity field that does not achieve a steady state, regardless of the integration time (as noticed by Wirth, 2020). This unsteady behavior is partly explained by the eigenvalues provided by the linear analysis: Some eigenvalues have in fact positive imaginary part and, therefore, the flow field is unstable. According to linear theory, the atmospheric state should diverge exponentially from the equilibrium state and each unstable Rossby wave should grow without bounds. The nonlinear simulation, however, does not

250

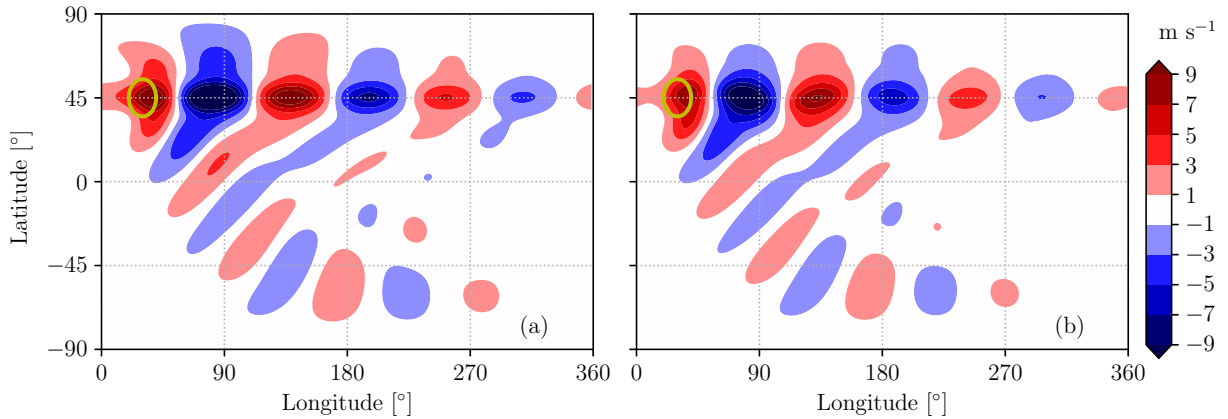


Figure 4. Meridional velocity in the strong-jet case ($U_J = 40 \text{ m s}^{-1}$) from the linear method at the equilibrium state (a). Meridional velocity field averaged between 10 and 100 days from the simulation start with the nonlinear solver (b). The circle indicates the topographic forcing.

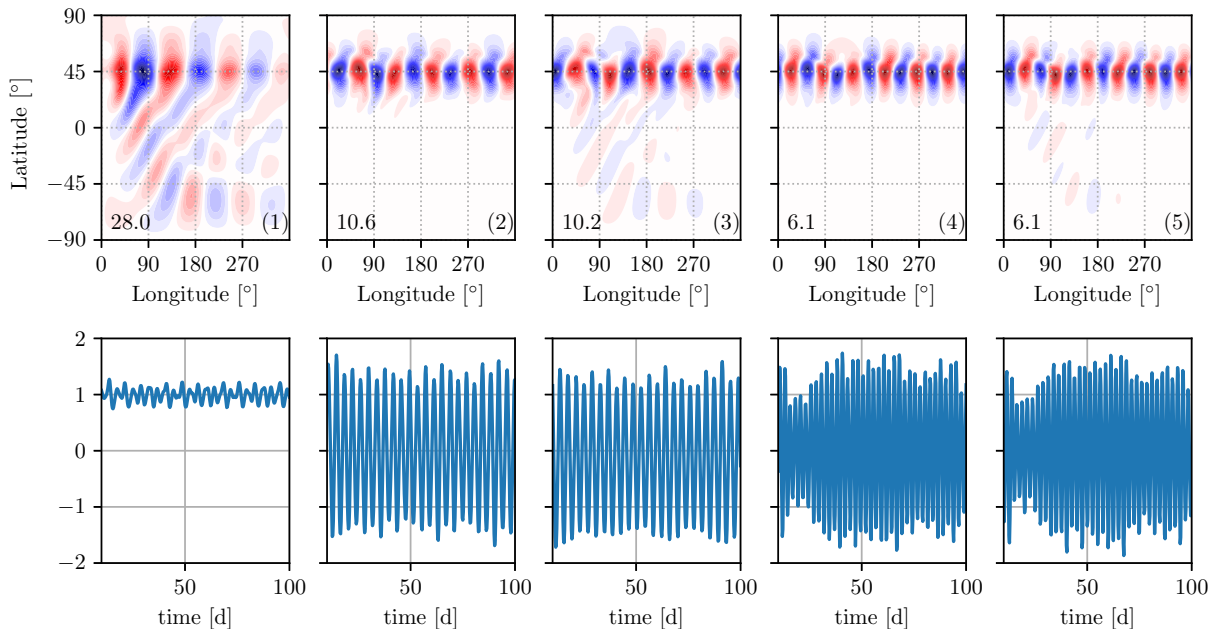


Figure 5. First five modes of the EOF decomposition of the meridional velocity field obtained from the nonlinear simulations (top) and their temporal coefficient normalized by their root mean square value (bottom) for the strong-jet case with $U_J = 40 \text{ m s}^{-1}$. The number in the bottom-left corner of the first row indicates the variance contribution of each mode. The color scale in the top row is not consistent between the different modes since each mode has unitary norm.

display such an unrealistic divergence of wave amplitudes. A great-circle wave propagation is still present as in the solid-body velocity case, as well as a wave pattern in the zonal direction of the waveguide corresponding to the strong jet (Fig. 4a).

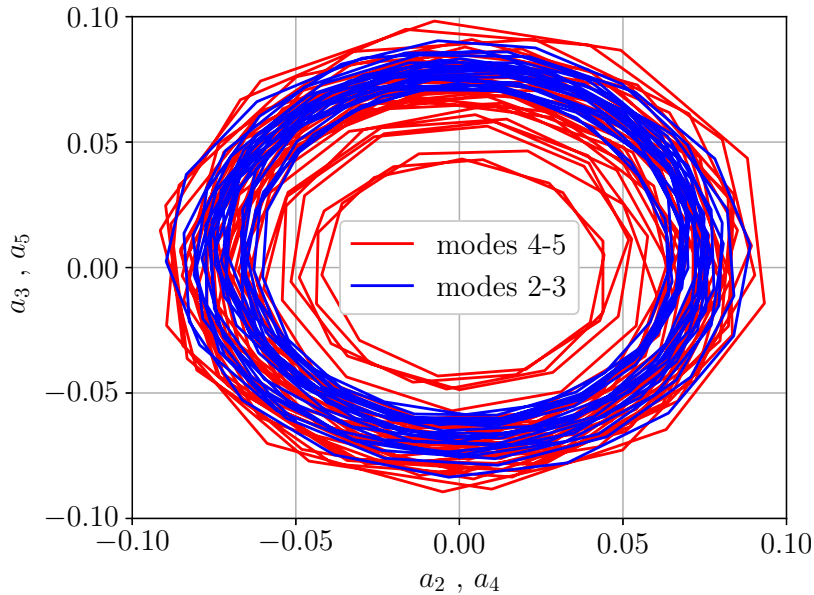


Figure 6. Evolution of the amplitude of mode 2 (4) plotted against the amplitude of mode 3 (5) from the EOF analysis shown in Fig. 5.

The linear eigenvalue analysis confirms that the equilibrium state given by Eq. (12) is indeed unstable. Nevertheless, such an unstable equilibrium state resembles quite closely the time-averaged nonlinear solution, which is bounded and characterized by the averaged field reported in Fig. 4b. Beyond the linearly stable range, only the nonlinear simulations could provide information about the flow evolution and whether or not an equilibrium state is achieved. In order to shed some light, an empirical orthogonal function (EOF) approach has been applied to the nonlinear simulation. The corresponding modes are shown in Fig. 5 to highlight the most energetic scales governing the temporal flow evolution. The first mode is practically constant in time and remains close to the time-averaged field of the nonlinear simulation, while the second-third, fourth-fifth, and sixth-seventh modes organize themselves to create traveling wave patterns with zonal wavenumbers $m = 5$, $m = 6$ and $m = 7$, respectively (the sixth-seventh modes are not shown). These first seven modes contain 60% of the meridional velocity variance. The modal coefficients of mode 2 and 3 are in quadrature with each other, and similarly happens for modes 4 and 5. The trajectories in the plane spanned by the corresponding principal components, shown in Fig. 6, belong to a closed orbit and behave as traveling waves: however, the linear stability analysis does not support this interpretation as the waves should grow exponentially in magnitude because they are unstable. A plausible alternative is that a limit cycle takes place (Strogatz, 2018): Since a limit cycle is associated with a nonlinearity of the system, a linear analysis cannot identify that, and this is consistent with the apparent divergence of the linear solution. The limit cycle orbits around the unstable equilibrium state of the system (provided by the first EOF mode), approximated in its linear version by Eq. (12).

Additional simulations where the orographic forcing was moved to lie right on the equator did not change this overall picture, and the traveling waves (i.e., the EOF modes after the mean component) remained at the jet latitude (not shown). This implies that the wave components described by the EOF analysis are traveling waves determined just by the background flow, rather

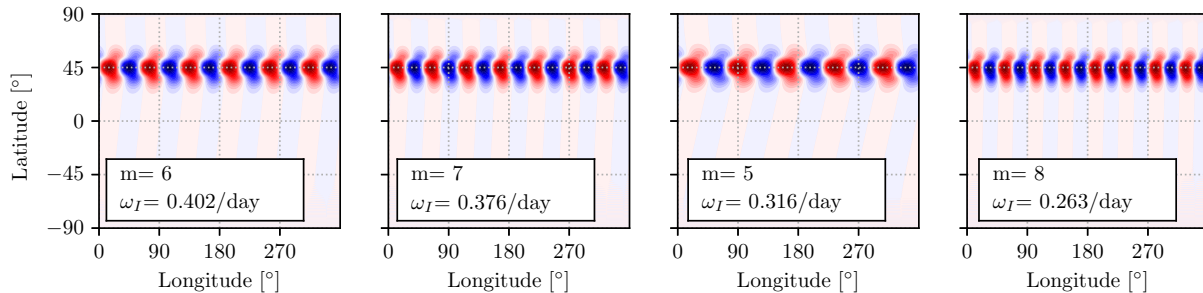


Figure 7. The 4 most unstable modes from the linear analysis sorted according to their growth rate in the strong-jet case.

than by the forcing, **similarly to what** suggested by the linear analysis. One might wonder if there is a correspondence between the unstable modes of the linear analysis and the most energetic EOF modes. The linear unstable waves are located at the jet latitude (Fig. 7) and have similar wavenumbers to the first EOF modes. Despite the similarity, however, the most-rapidly growing mode ($m = 6$, Fig. 7) does not exactly match the EOF patterns corresponding to the modes 2 and 3 (which appear to project on $m = 5$, cf. Fig. 5). We will further delve on the factors determining the shape of the unstable modes in the next section.

4.3 Stability analysis

We conduct here a systematic stability analysis to identify at which jet velocity and width unsteady traveling-wave patterns begin to appear. **The Rayleigh stability criterion provides a necessary condition for the onset of barotropic instability, namely a change in sign of the absolute vorticity gradient $\partial(\bar{\zeta} + 2\Omega a \cos\theta)/\partial\theta$.** The derivation of the criterion can be applied to Eq. (9) leading to the result that, whenever the absolute vorticity gradient changes sign, it is possible that the imaginary part of ω is different from $-\chi$, with a significant stability margin before the actual onset of the linear instability (namely when the imaginary part of ω becomes positive). This results pinpoints the role of dissipation in retarding the onset of barotropic instability, confirming that the Rayleigh criterion provides a necessary but not sufficient condition for the onset of instability (Kuo, 1949).

Let us consider first the results of the **eigenvalue** analysis for a narrow jet zonal profile ($\sigma_J = 5^\circ$; blue dots in Fig. 8) over an array of different jet speed U_J and latitude φ_J . At low U_J the imaginary part of the most unstable eigenvalue is determined by the dissipation parameter χ . **This is valid as long as the absolute vorticity gradient has the same sign.** As U_J increases, the stability margin decreases: above $15\text{--}22 \text{ m s}^{-1}$ at least one eigenvalue becomes positive, leading to the divergence of the linear solution with a growth rate directly proportional to the jet velocity. **Nonlinear simulations follow a similar pattern, but the solution approaches an unstable state for larger jet velocity than for the linear method (as indicated by the green line in figure 8a).** Above this threshold, the vorticity variance increases drastically and it is concentrated at the jet location irrespective of the forcing, indicating the onset of the limit cycle. The neutral curve from the linear stability analysis is then a conservative estimate of the onset of instability, when compared to the onset of unsteady fluctuations in the nonlinear analysis. This underlines once

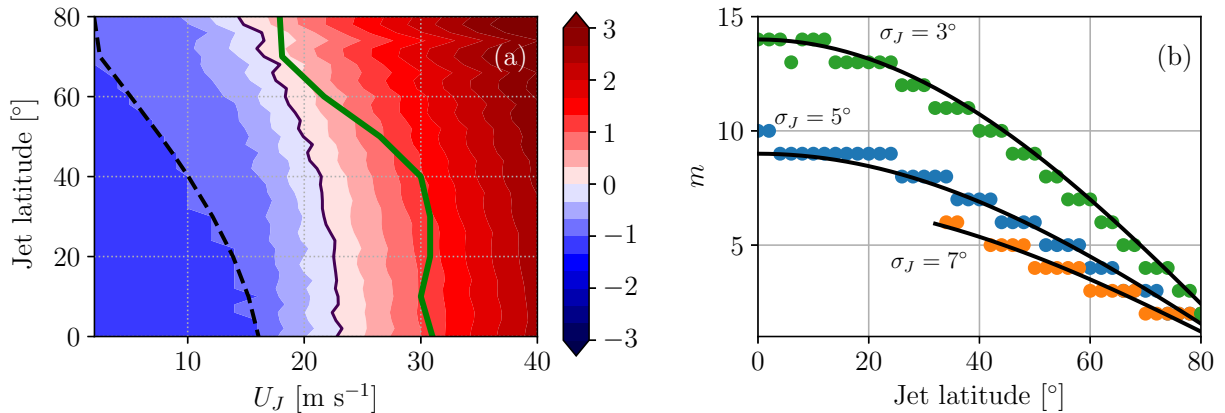


Figure 8. (a) Maximum of the imaginary part of the linear eigenvalues for a given jet velocity (normalised by χ) when $\sigma_J = 5^\circ$. The black line indicates the neutral curve, the dashed line is the locus where the absolute vorticity gradient changes sign (Rayleigh stability criterion), while the green thick line is the locus beyond which the temporal vorticity variance of the nonlinear simulation becomes 10 times larger than in the stable regimes (equivalent to the neutral curve in the nonlinear case). (b) Azimuthal wavenumber of the most unstable eigenvalue for $U_J = 40 \text{ m s}^{-1}$ for different jet widths and latitudes. The black lines are curves $m \propto \cos \varphi_J$ fitting the linear stability results.

again the stabilizing role of nonlinear terms not included in the linear method, such as wave-wave interaction. A weaker jet velocity is needed for the instability onset when the jet approaches the pole where the linear and nonlinear neutral curves are close to each other.

It is also interesting to monitor the wavenumber associated with the most unstable eigenvalue. After the onset of the linear instability, this wavenumber does not depend on U_J , and therefore the maximum growth rate in Fig. 8b is only shown for $U_J = 40 \text{ m s}^{-1}$, where the jet is unstable at all latitudes. For $\varphi_J = 45^\circ\text{N}$ a wavenumber $m = 6$ is the most unstable, similar to what pointed out by the EOF analysis. However, as the jet is shifted to the pole, the most unstable wavenumber systematically decreases following the cosine of φ_J . It is possible to explain this trend by assuming that the instability is associated with a wavelength independent of the latitude, given by

$$L = \frac{2\pi}{m} a \cos \varphi = \text{constant}, \quad (19)$$

which is indeed proportional to $\cos \varphi$. This implies that the most barotropically-unstable Rossby wave has the same wavelength at different latitudes of the zonal jet. Inspired by the analysis of Gill (1982), it is expected that the Rossby wave will become more unstable for narrower jet width, σ_J , and conversely less unstable for a wider jet. Fig. 8b shows also the zonal wavenumber of the most unstable mode for $U_J = 40 \text{ m s}^{-1}$ and three different jet widths ($\sigma_J = 3^\circ, 5^\circ$ and 7°). In general, the wavelength of the most unstable mode becomes larger as the jet latitude increases. However, modes associated with a narrow jets exhibit a higher wavenumber than for a broad jet ($\sigma_J = 7^\circ$). Interestingly, the broader jet is unstable only when the jet is far enough from the equator and it is stable for $\varphi_J < 30^\circ\text{N}$. By having the even higher value $\sigma_J = 10^\circ$, the instability disappears at all jet latitudes and the flow becomes stable again at $U_J = 40 \text{ m s}^{-1}$ (not shown).

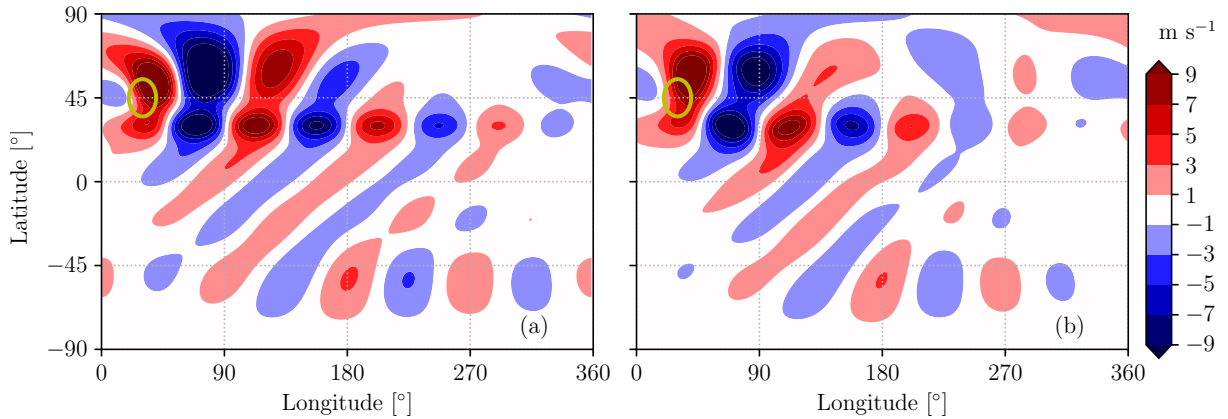


Figure 9. Meridional velocity associated with a zonal jet characterized by $U_J = 40 \text{ m s}^{-1}$ with $\varphi_J = 30^\circ\text{N}$ at the equilibrium state from the linear analysis (a) and averaged between 10 and 100 days from the simulation start with the nonlinear solver (b).

5 The double-jet case

315 After having considered the single-jet case, we now consider a configuration with two separate jets of width $\sigma_J = 5^\circ$ located at different latitudes. The double-jet setup was chosen as it is representative of the interplay between the subtropical and the eddy-driven jet streams observed in the Northern Hemisphere, and because recent research has connected it to the occurrence of quasi-stationary Rossby waves and summer heat extremes (Rousi et al., 2022). The first jet is located at $\varphi_J = 30^\circ\text{N}$ and has a jet velocity of $U_J = 40 \text{ m s}^{-1}$ (the associated perturbation field is shown in Fig. 9 once again for both the linear and nonlinear
320 simulation). The second jet is located at $\varphi_J = 60^\circ\text{N}$ and has also a jet velocity of $U_J = 40 \text{ m s}^{-1}$ (the associated perturbation field is shown in Fig. 10).

The perturbations resulting from the 30°N jet feature a combination of great-circle and along-jet propagation, that is properly represented by both the linear and nonlinear approaches (Fig. 9). On the other hand, for the jet at 60°N the along-jet propagation is obtained only in the linear simulation, while it is much weaker in the nonlinear simulation (Fig. 10). The weakening of along-
325 jet propagation can be due to an enhanced equatorward propagation of the stationary wave in the nonlinear case, given that the forcing is located at 45°N , possibly combined with enhanced dissipation. **By using Eq. (18), the waveguidability of the 30°N jet is 84% while the one of the 60°N jet is 92%, highlighting that jets with same velocity act as equally efficient waveguides.**

Moving to the double-jet configuration we notice, first of all, a good agreement between the linear and the nonlinear solution (Fig. 11). Rossby wave propagation occurs separately along the waveguides delineated by the two jet streams, while great-
330 circle propagation to the Southern Hemisphere is smaller in the double-jet configuration than for the jets taken individually. The double-jet pattern corresponds roughly to the combination of the patterns of the linear solutions for the two individual jets. However, this is not true for the nonlinear solutions, because of the previously discussed lack of Rossby wave propagation along the 60°N jet in the nonlinear single-jet case. It might be that forced meridional velocity perturbations along the 30°N jet stream could provide energy to the jet at 60°N , which would otherwise be attenuated as in the single-jet case (Fig. 11b):

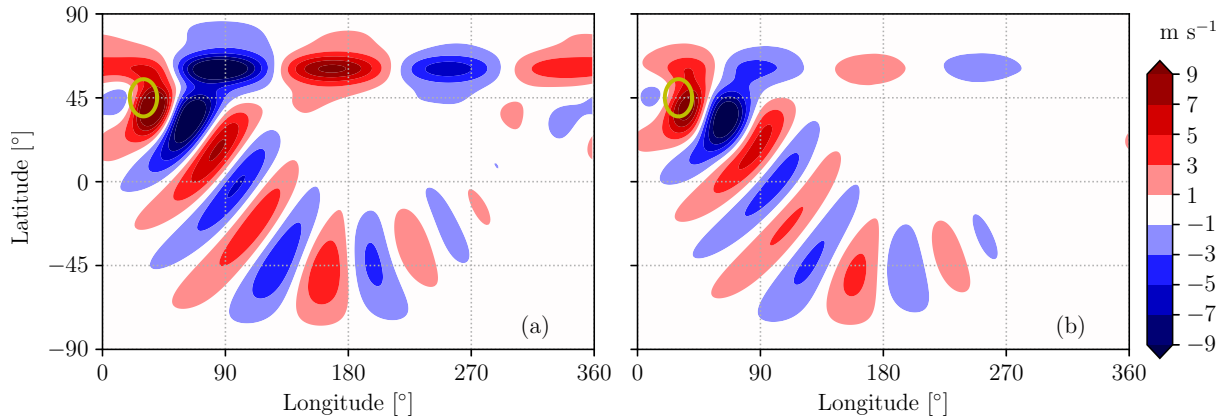


Figure 10. Meridional velocity associated with a zonal jet characterized by $U_J = 40 \text{ m s}^{-1}$ with $\varphi_J = 60^\circ\text{N}$ at the equilibrium state from the linear analysis (a) and averaged between 10 and 100 days from the simulation start with the nonlinear solver (b).

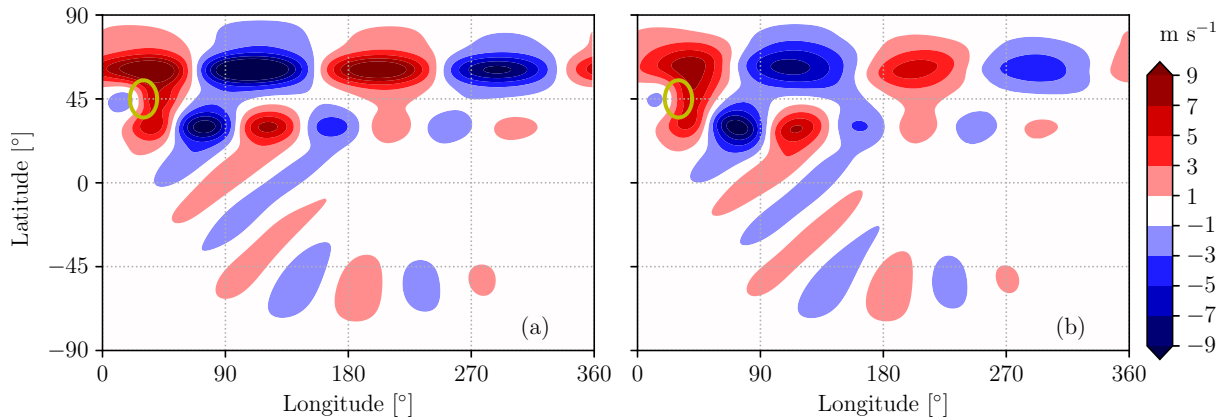


Figure 11. Meridional velocity associated with two zonal jets ($U_{J,1} = 40 \text{ m s}^{-1}$ with $\varphi_{J,1} = 30^\circ\text{N}$ and $U_{J,2} = 40 \text{ m s}^{-1}$ with $\varphi_{J,2} = 60^\circ\text{N}$) at the equilibrium state from the linear analysis (a) and averaged between 10 and 100 days from the simulation start with the nonlinear solver (b).

335 However, this hypothesis would need further verification. Furthermore, the waveguidability of the two jets is lower than the one
of the two distinct jets: the 30°N jet has waveguidability of 70%, while the 60°N jet has a value of 82%. The waveguidability
of the 60°N jet has been estimated using Eq. (18), considering a fictitious forcing centered at 60°N and by monitoring the
enstrophy anomaly around the same latitude (and similarly for the 30°N jet). The fact that the waveguidability is reduced by
10% for both jets is probably due to the jet streams' ability to attract leaked enstrophy from the surrounding regions (including
340 the other jet stream), making the two jets more leaky than the ideal waveguides. However, the reader is warned that these results
are likely sensitive to the choice of the reference state in Eq. (18) (here taken as the solid-body background flow).

6 Time-dependent solution

The discussions in the previous sections have mostly focused on the equilibrium condition and on its stability. However, as discussed in the appendix, the modal solution allows also a transient analysis, tracking the evolution of the waves as they develop. Let us consider for instance a weak single-jet case with $U_J = 20 \text{ m s}^{-1}$ and $\varphi_J = 45^\circ\text{N}$. Fig. 12 shows a comparison between the time evolution of the wave obtained by using the linear method and the nonlinear model, as the Gaussian mountain is introduced at the initial time. The high resemblance of the two solutions is visible for the first 100 hours and maintained throughout the length of the simulations, although the meridional wind anomalies in the nonlinear simulation appear slightly weaker and smoother. Beyond 500 hours both simulations achieve a steady state. This is to be expected, since the linear analysis indicated that all the eigenvalues had a negative imaginary part and, thus, the system is stable (see Sec. 4.3 for a detailed discussion of the neutral curve). The result is a stationary wave train originating from the interaction of the jet with the topography, featuring both a degree of great-circle and of along-jet propagation.

7 Conclusions

A linearised framework is proposed to solve the barotropic vorticity equation and determine the Rossby wave response to topographic forcing in different background flow configurations. First the homogeneous solution is obtained by introducing a modal assumption in the zonal direction and temporal coordinate. This leads to an eigenvalue problem where the eigenfunctions are modes in the meridional direction. From the eigenvalues it is possible to assess the mode stability by looking at the sign of the imaginary part (a positive value indicates linear instability and exponential growth of the mode when triggered). The forced case is treated as an initial value problem but the solution is now much facilitated by the modal analysis of the homogeneous equation and no numerical integration nor additional modal analysis is required. **In distinct contrast to ray-tracing theory, the present approach has general validity for any background flow and forcing combination, does not require projecting the flow field on a Mercator plane and does not assume any scale separation between the background flow and the waves. Such an approach additionally provides information on the time evolution of the wave.**

The proposed linear framework has been compared with nonlinear simulations performed with a spectral code based on spherical harmonics. The analysis of the jet waveguidability showed small quantitative differences between the linearised solution and the nonlinear simulations. Strong-jet cases, characterized by unstable eigenvalues, showed a different **temporal** behavior from the expected divergence of the linear solution. The flow field did not diverge exponentially, instead **it started** oscillating around the unstable equilibrium state. This dynamics was further investigated by means of empirical orthogonal functions, showing that modes with an azimuthal wavenumber of 5 up to 7 are associated with traveling waves and a limit cycle, a dynamics **originated** by nonlinear effects. Nevertheless, the averaged flow field in the nonlinear simulation resembles (equally well as for other stable cases) the unstable equilibrium state calculated from the linear method. The latter is an equilibrium state obtained by removing the time derivative and is therefore an approximation of the equilibrium condition of the nonlinear system too. The correspondence between linear method and nonlinear simulations is not just restricted to the center of the limit cycle (i.e. the mean of the atmospheric state), but also to the other EOF modes. This was verified by comparing higher EOF

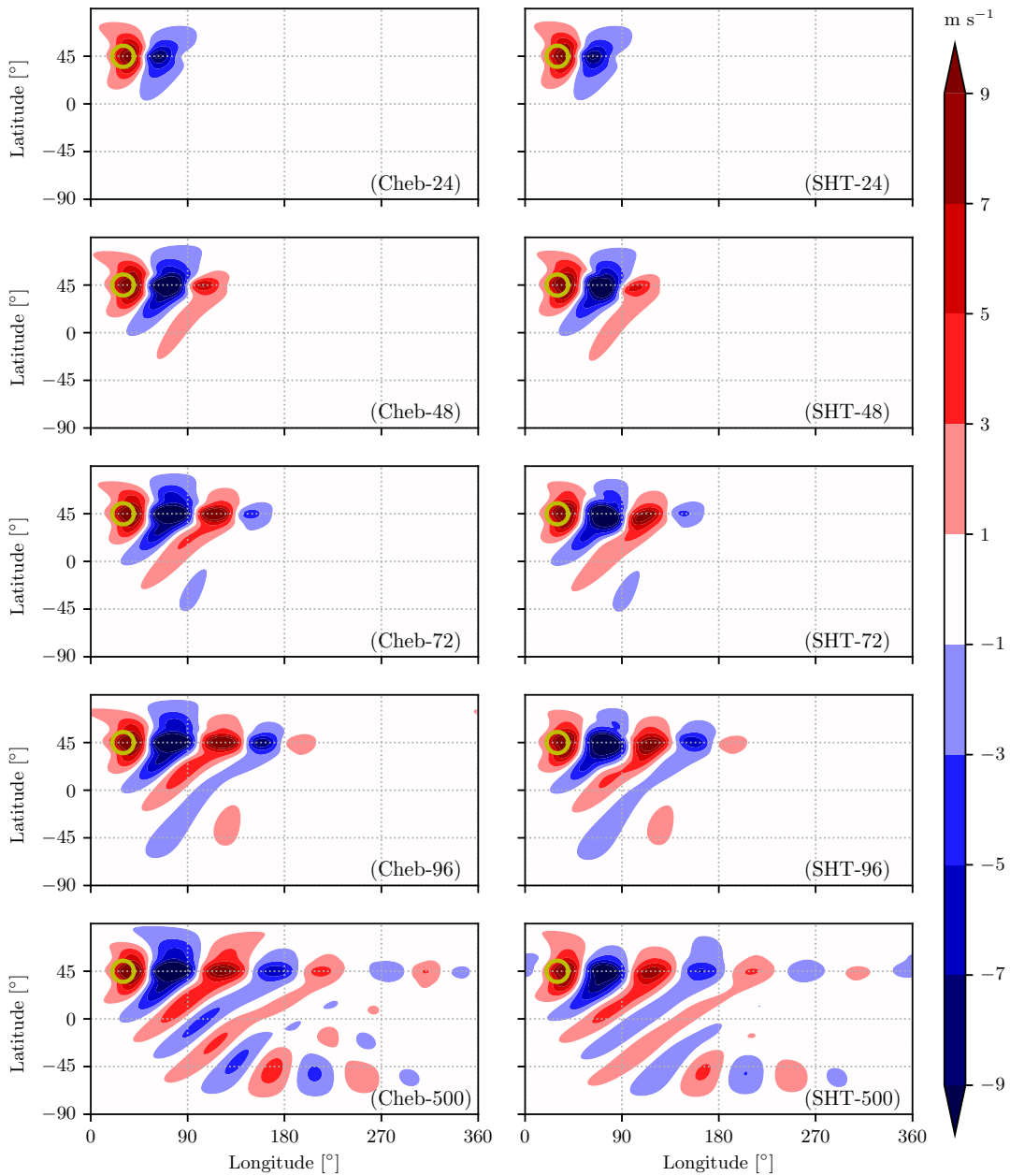


Figure 12. Meridional velocity patterns at different times from the linear analysis (left) and the nonlinear solver (right) for a jet located at $\varphi_J = 45^\circ\text{N}$ and $U_J = 20 \text{ m s}^{-1}$. The circle indicates the topographic forcing, switched on at $t = 0 \text{ h}$. The actual time of the simulation (in hours) is indicated in the brackets.

375 modes with the unstable modes from the linear analysis, and the two showed good resemblance. **This indicates that the linear analysis provides valuable information about both the steady and the transient parts of the flow.**

The equilibrium state obtained from the linearized analysis can be employed to quantify the waveguidability for a variety of background flow configurations. A new definition of waveguidability, based on a zonal average of the enstrophy anomaly, has been proposed in the present work. We reconfirmed earlier results that jet waveguidability is strongly related to jet speed, and we showed that jet latitude plays a considerably smaller role.

As the emergence of barotropic instability would violate the assumption of linearity, we also performed a stability analysis to identify the limits of applicability of the linear method. We noticed that the change of sign in the absolute vorticity gradient (i.e., the Rayleigh criterion) was not capable of detecting the onset of barotropic instability, which was observed at higher jet speeds than expected. In the linear framework, the condition of instability corresponded to a first increase of the (still negative) imaginary part of the eigenvalues from the negative value set by the attenuation parameter. Instability arose only at larger jet velocity, when the complex part of the eigenvalue actually turned positive. The analysis neatly isolates the effect of dissipative conditions onto the onset of barotropic instability. Even more intriguing, nonlinear simulations started showing signs of barotropic instability even later than what the linear neutral curve suggested, pointing to potential damping effects operated by nonlinear terms (e.g., wave-wave interactions). This was also observed from the spatial distribution of the wave, that appeared always smoother in the nonlinear simulations compared to the linear method (ruling out possible differences in the numerical diffusion). It seems thus clear that linear instability is necessary to observe the emergence of nonlinear instability, but not sufficient.

The stability analysis also allowed us to estimate the preferred azimuthal wavenumber of the moving Rossby wave train associated with the barotropic instability. The wavenumber decreases with jet latitude and is only weakly dependent on the jet intensity. For jet streams located in the mid-latitudes, typical values of the azimuthal wavenumbers of 5-7 are observed. A high sensitivity of the preferred azimuthal mode and of the instability onset was instead observed for different jet widths. Very narrow jet widths promote higher growth rates and shorter wavelengths, in agreement with the link between vorticity gradients and instability.

The application of the proposed approach to a double-jet configuration indicates that: a) the equatorward propagation of Rossby waves is weakened in a double-jet case compared to the no-jet case; b) the double-jet response roughly corresponds to the linear combination of the individual jet responses; and c) that the waveguidability of each jet seems to be higher than when the two jets occur in a double-jet configuration. The possibility of an interaction between the wave trains associated with the two jets cannot be ruled out, especially if the two are not located sufficiently far apart. These results indicate the need of a more targeted analysis of Rossby wave propagation in presence of multiple jets, together with the development of appropriate metrics to quantify waveguidability in such circumstances.

We envisage several future applications of our analysis approach. For example, a systematic waveguidability assessment for different forcings and background zonal wind profiles, including a detailed investigation of double-jet configurations. Another relevant application would be to understand the role of orography in forcing Rossby waves with specific zonal wavenumbers, as amplified waves of specific wavenumbers have been related to surface weather extremes during summer (as noticed, among others, by Coumou et al., 2014; Jiménez-Esteve et al., 2022). Although we do not attempt this here, these evidences could enable building a reduced-order model of a barotropic atmosphere where the spatial modes are provided by the equilibrium

state and by the most unstable modes (this information being retrieved exclusively from the linear analysis), while the temporal coefficients could be determined by solving a small set of nonlinear ordinary differential equations (Holmes et al., 2012).

415 In conclusion, we present a relatively simple and computationally efficient way to study the steady and unsteady Rossby wave response to topography in a variety of idealized background flow configurations. This approach goes beyond a number of limitations of ray-tracing theory for determining waveguidability, and we have illustrated the physical insights it can provide by considering a wide parameter sweep of jet speeds and latitudes and a double-jet configuration.

Appendix A: Spectral solution of the barotropic vorticity equation

Equation (10) introduces the Laplace operator \mathcal{L} in the transformed space together with the boundary conditions needed to avoid the pole singularity

$$\widehat{\psi}(\theta = 0) = 0 \quad \text{for} \quad m \neq 0 \quad \text{and} \quad \left. \frac{\partial \widehat{\psi}}{\partial \theta} \right|_{\theta=0} = 0 \quad \text{for} \quad m \neq \pm 1, \quad (\text{A1})$$

and similarly for $\theta = \pi$. Consequently, there are two boundary conditions for $|m| \leq 1$ and four otherwise. An additional boundary condition must be introduced at $m = 0$ as $\widehat{\psi}(\theta = 0) = 0$ in order to set the value of the streamfunction at one pole since, otherwise, the streamfunction would be defined up to an additive constant, making the numerical problem singular.

425 Following Peyret (2002), the solution of Eq. (9) is calculated by a spectral collocation method in terms of orthogonal polynomials. In the present work, Chebyshev polynomials, $T_q(\theta)$, and the decomposition

$$\widehat{\psi}(\theta, t; m) \approx \sum_{q=0}^N a_q(t; m) T_q(\theta), \quad (\text{A2})$$

are used. The $N + 1$ collocation points are described by a shifted Gauss-Lobatto distribution

$$\theta_j = \frac{\pi}{2} \left[1 - \cos \left(\pi \frac{j}{N} \right) \right] \quad \text{with} \quad j \in \{0, 1, \dots, N-1, N\}, \quad (\text{A3})$$

430 implying a refinement of the colatitude distribution near the poles. This is in contrast with the Legendre and associated Legendre polynomials that account for a more appropriate resolution at the poles. Nevertheless, Chebyshev polynomials have been preferred here since an exact method to calculate the spectral coefficients exists for them, while the Legendre polynomials require a numerical quadrature scheme (Krishnamurti et al., 2006). **The choice of the specific family of polynomials influences only the derivatives in the meridional direction and the meridional discretization, while the zonal discretization is still based on the Fourier transform as is the case for spherical harmonics.**

Rather than working with the spectral coefficients, $a_q(t; m)$, here it is preferred to work directly with the value of the streamfunction at the collocation points, $\widehat{\psi}_j = \widehat{\psi}(\theta_j, t; m)$, as unknowns collected into a vector, significantly facilitating the interpretation of the results. The derivatives of the streamfunction are calculated as

$$\left. \frac{\partial \widehat{\psi}}{\partial \theta} \right|_j \approx D^{(1)} \widehat{\psi}_j, \quad \left. \frac{\partial^2 \widehat{\psi}}{\partial \theta^2} \right|_j \approx D^{(2)} \widehat{\psi}_j, \quad (\text{A4})$$

440 where the matrices $D^{(1)}$ and $D^{(2)}$ provide the first- and second-order derivatives (Peyret, 2002). Another advantage of the Chebyshev basis is that the matrices $D^{(1)}$ and $D^{(2)}$ are analytically known (Peyret, 2002; Canuto et al., 2006), although some modifications to limit the effect of round-off errors have been implemented (Bayliss et al., 1995).

By exploiting Eq. (A4), the discretized Laplace operator becomes

$$\mathcal{L} \approx D^{(2)} + \cot \theta D^{(1)} - \frac{m^2}{\sin^2 \theta} I, \quad (\text{A5})$$

445 where I indicates the identity matrix. This implies that the Laplace operator becomes a numerical matrix since the spatial dependence of the variables is provided by the Fourier modes (in the zonal direction) and by the Chebyshev polynomials (in the meridional direction). Once the Laplace operator has been discretized, the matrices A and B in equation (11) are obtained from their definition.

As stated in Eq. (A1), the boundary conditions at the poles have been imposed by removing 2, 3 or 4 points from the analysis
 450 so that the size of the matrices A or B is $N - 2 \times N - 2$ for $m = 0$, $N - 1 \times N - 1$ for $|m| = 1$ and $N - 3 \times N - 3$ otherwise. This has the advantage that the reduced forms of A and B are just related to the dynamics of the modeled system rather than the boundary conditions (the reader is referred to section 3.7.1 of Peyret, 2002, for a detailed description on how the matrices can be reduced), together with a decrease of the computational cost.

If B is nonsingular, it is possible to perform the eigendecomposition $B^{-1}A = P\Lambda P^{-1}$ where the columns of P are the
 455 eigenvectors and Λ is a diagonal eigenvalue matrix. The analytical solution of Eq. (11) is found to be

$$\widehat{\psi}_j(t; m) = Pe^{-i\Lambda t} \left[P^{-1}\widehat{\psi}_j(0; m) + i \int_0^t e^{i\Lambda\tau} P^{-1}B^{-1}\widehat{F}(\tau) d\tau \right], \quad (\text{A6})$$

with $\widehat{\psi}_j(0; m)$ indicating the initial condition of the streamfunction. In the special case of a steady forcing, Eq. (A6) becomes

$$\widehat{\psi}_j(t; m) = Pe^{-i\Lambda t} P^{-1}\widehat{\psi}_j(0; m) + (I - Pe^{-i\Lambda t} P^{-1}) A^{-1}\widehat{F}. \quad (\text{A7})$$

The first term of Eq. (A6) and (A7) is the homogeneous unforced solution of the linear system with initial condition $\widehat{\psi}_j(0; m)$,
 460 while the second term is the forced solution with zero initial condition.

Since the eigenvalues, Λ , and eigenfunctions, P , depend on the zonal velocity, U , Rossby number, Ro , and wavenumber, m , they are calculated and stored for all the considered wavenumbers for a given zonal velocity profile and Rossby number. Since they do not depend on the actual forcing applied, once they are computed they can be used with any kind of forcing according to Eqs. (A6-A7). Furthermore, since the equation is linear, no aliasing instability is present and each eigenmode does not interact
 465 with the others. **Equation (A6) enables the calculation of the solution at any time without the need for numerical integration. This is nevertheless necessary if the forcing is time dependent, although with a definite integral instead.**

Author contributions. AS developed the theory, performed the simulations shown in the manuscript and analyzed the data. All authors contributed equally to the interpretation of the results. AS and JR prepared the manuscript, assisted by GM and VW for review and editing.

Competing interests. The authors declare that no competing interests are present.

470 References

- Ambrizzi, T., Hoskins, B. J., and Hsu, H.-H.: Rossby Wave Propagation and Teleconnection Patterns in the Austral Winter, *J. Atmos. Sci.*, 52, 3661–3672, [https://doi.org/10.1175/1520-0469\(1995\)052<3661:RWPATP>2.0.CO;2](https://doi.org/10.1175/1520-0469(1995)052<3661:RWPATP>2.0.CO;2), 1995.
- Baldauf, M. and Brdar, S.: An analytic solution for linear gravity waves in a channel as a test for numerical models using the non-hydrostatic, compressible Euler equations, *Quart. J. Roy. Meteor. Soc.*, 139, 1977–1989, <https://doi.org/https://doi.org/10.1002/qj.2105>, 2013.
- 475 Bayliss, A., Class, A., and Matkowsky, B. J.: Roundoff error in computing derivatives using the Chebyshev differentiation matrix, *J. Comput. Phys.*, 116, 380–383, 1995.
- Boyd, J. P.: The Effects of Latitudinal Shear on Equatorial Waves. Part I: Theory and Methods, *J. Atmos. Sci.*, 35, 2236–2258, [https://doi.org/10.1175/1520-0469\(1978\)035<2236:TEOLSO>2.0.CO;2](https://doi.org/10.1175/1520-0469(1978)035<2236:TEOLSO>2.0.CO;2), 1978.
- Branstator, G.: Circumglobal teleconnections, the jet stream Waveguide, and the North Atlantic Oscillation, *J. Climate*, 15, 1893–1910, [https://doi.org/10.1175/1520-0442\(2002\)015<1893:CTTJSW>2.0.CO;2](https://doi.org/10.1175/1520-0442(2002)015<1893:CTTJSW>2.0.CO;2), 2002.
- 480 Brayshaw, D. J., Hoskins, B., and Blackburn, M.: The basic ingredients of the North Atlantic Storm Track. Part I: Land–Sea contrast and orography, *J. Atmos. Sci.*, 66, 2539–2558, <https://doi.org/10.1175/2009JAS3078.1>, 2009.
- Campbell, L. and Maslowe, S.: Forced Rossby wave packets in barotropic shear flows with critical layers, *Dynamics of Atmospheres and Oceans*, 28, 9–37, [https://doi.org/https://doi.org/10.1016/S0377-0265\(98\)00044-X](https://doi.org/https://doi.org/10.1016/S0377-0265(98)00044-X), 1998.
- 485 Canuto, C., Hussaini, M. Y., Quarteroni, A., and Zang, T. A.: Spectral methods. Fundamentals in single domains., *Sci. Comput.*, Berlin: Springer, <https://doi.org/10.1007/978-3-540-30726-6>, 2006.
- Coumou, D., Petoukhov, V., Rahmstorf, S., Petri, S., and Schellnhuber, H. J.: Quasi-resonant circulation regimes and hemispheric synchronization of extreme weather in boreal summer, *Proc. Nat. Academy Sci.*, 111, 12 331–12 336, <https://doi.org/10.1073/pnas.1412797111>, 2014.
- 490 Davies, H.: Weather chains during the 2013/2014 winter and their significance for seasonal prediction, *Nature Geosci.*, 8, 833–837, <https://doi.org/10.1038/ngeo2561>, 2015.
- Di Capua, G., Sparrow, S., Kornhuber, K., Rousi, E., Osprey, S., Wallom, D., van den Hurk, B., and Coumou, D.: Drivers behind the summer 2010 wave train leading to Russian heatwave and Pakistan flooding, *npj Climate and Atmospheric Science*, 4, 1–14, 2021.
- Garcia, R. R. and Salby, M. L.: Transient response to localized episodic heating in the tropics. Part II: Far-field behavior, *J. Atmos. Sci.*, 44, [499–532](https://doi.org/10.1175/1520-0469(1987)044<499:TRTELE>2.0.CO;2), 1987.
- 495 Garfinkel, C. I., White, I., Gerber, E. P., Jucker, M., and Erez, M.: The building blocks of Northern Hemisphere wintertime stationary waves, *J. Climate*, 33, 5611–5633, <https://doi.org/10.1175/JCLI-D-19-0181.1>, 2020.
- Gill, A. E.: *Atmosphere-ocean dynamics*, vol. 30, Academic press, 1982.
- Harnik, N., Messori, G., Caballero, R., and Feldstein, S. B.: The Circumglobal North American wave pattern and its relation to cold events [in eastern North America](https://doi.org/https://doi.org/10.1002/2016GL070760), *Geophys. Res. Lett.*, 43, 11,015–11,023, <https://doi.org/https://doi.org/10.1002/2016GL070760>, 2016.
- 500 Haurwitz, B.: The motion of atmospheric disturbances on the spherical earth, *J. mar. Res.*, 3, 254–267, 1940.
- Held, I. M.: Stationary and quasi-stationary eddies in the extratropical troposphere: Theory, in: *Large-Scale Dynamical Processes in the Atmosphere*, edited by Hoskins, B. J. and Pearce, R. P., pp. 127–168, Academic Press, 1983.
- Held, I. M., Ting, M., and Wang, H.: Northern Winter Stationary Waves: Theory and Modeling, *J. Climate*, 15, 2125–2144, [https://doi.org/10.1175/1520-0442\(2002\)015<2125:NWSWTA>2.0.CO;2](https://doi.org/10.1175/1520-0442(2002)015<2125:NWSWTA>2.0.CO;2), 2002.
- 505

- Holmes, P., Lumley, J. L., Berkooz, G., and Rowley, C. W.: Turbulence, coherent structures, dynamical systems and symmetry, Cambridge university press, 2012.
- Hoskins, B. and Woollings, T.: Persistent Extratropical Regimes and Climate Extremes, *Curr. Climate Change Rep.*, 1, 115–124, <https://doi.org/10.1007/s40641-015-0020-8>, 2015.
- 510 Hoskins, B. J. and Ambrizzi, T.: Rossby Wave Propagation on a realistic longitudinally varying flow, *J. Atmos. Sci.*, 50, 1661–1671, [https://doi.org/10.1175/1520-0469\(1993\)0502.0.CO;2](https://doi.org/10.1175/1520-0469(1993)0502.0.CO;2), 1993.
- Hoskins, B. J. and Karoly, D. J.: The steady linear response of a spherical atmosphere to thermal and orographic Forcing, *J. Atmos. Sci.*, 38, 1179–1196, [https://doi.org/10.1175/1520-0469\(1981\)038<1179:TSLROA>2.0.CO;2](https://doi.org/10.1175/1520-0469(1981)038<1179:TSLROA>2.0.CO;2), 1981.
- Hoskins, B. J. and Valdes, P. J.: On the existence of Storm-Tracks, *J. Atmos. Sci.*, 47, 1854–1864, [https://doi.org/10.1175/1520-0469\(1990\)047<1854:OTEOST>2.0.CO;2](https://doi.org/10.1175/1520-0469(1990)047<1854:OTEOST>2.0.CO;2), 1990.
- 515 Jiménez-Esteve, B., Kornhuber, K., and Domeisen, D. I. V.: Heat Extremes Driven by Amplification of Phase-Locked Circumglobal Waves Forced by Topography in an Idealized Atmospheric Model, *Geophys. Res. Lett.*, 49, e2021GL096337, <https://doi.org/10.1029/2021GL096337>, 2022.
- Kalnay, E.: Atmospheric modeling, data assimilation and predictability, Cambridge university press, 2003.
- 520 Kornhuber, K., Osprey, S., Coumou, D., Petri, S., Petoukhov, V., Rahmstorf, S., and Gray, L.: Extreme weather events in early summer 2018 connected by a recurrent hemispheric wave-7 pattern, *Environ. Res. Lett.*, 14, 054 002, <https://doi.org/10.1088/1748-9326/ab13bf>, 2019.
- Krishnamurti, T. N., Bedi, H., Hardiker, V., and Watson-Ramaswamy, L.: An introduction to global spectral modeling, vol. 35, Springer Science & Business Media, 2006.
- Kuo, H.-I.: Dynamic instability of two-dimensional nondivergent flow in a barotropic atmosphere, *Journal of Atmospheric Sciences*, 6, 105–122, 1949.
- 525 Manola, I., Selten, F., de Vries, H., and Hazeleger, W.: “Waveguidability” of idealized jets, *J. Geophys. Res.: Atmospheres*, 118, 10,432–10,440, <https://doi.org/10.1002/jgrd.50758>, 2013.
- Martius, O., Schwierz, C., and Davies, H. C.: Tropopause-Level Waveguides, *J. Atmos. Sci.*, 67, 866–879, <https://doi.org/10.1175/2009JAS2995.1>, 2010.
- 530 Martius, O., Wehrli, K., and Rohrer, M.: Local and remote atmospheric Responses to Soil Moisture Anomalies in Australia, *J. Climate*, 34, 9115–9131, <https://doi.org/10.1175/JCLI-D-21-0130.1>, 2021.
- Petoukhov, V., Rahmstorf, S., Petri, S., and Schellnhuber, H. J.: Quasiresonant amplification of planetary waves and recent Northern Hemisphere weather extremes, *Proc. Nat. Acad. Sci.*, 110, 5336–5341, <https://doi.org/10.1073/pnas.1222000110>, 2013.
- Peyret, R.: Spectral methods for incompressible viscous flow, vol. 148, New York, NY: Springer, 2002.
- 535 Rhines, P. B.: Waves and turbulence on a beta-plane, *J. Fluid Mech.*, 69, 417–443, 1975.
- Rossby, C.-G.: Relation between variations in the intensity of the zonal circulation of the atmosphere and the displacements of the semi-permanent centers of action, *J. Marine Res.*, 2, 38–55, 1939.
- Rossby, C.-G.: Planetary flow patterns in the atmosphere, *Quart. J. Roy. Meteor. Soc.*, 66, 68–87, 1940.
- Rousi, E., Kornhuber, K., Beobide-Arsuaga, G., Luo, F., and Coumou, D.: Accelerated western European heatwave trends linked to more-persistent double jets over Eurasia, *Nature communications*, 13, 1–11, 2022.
- 540 Schaeffer, N.: Efficient spherical harmonic transforms aimed at pseudospectral numerical simulations, *Geochemistry, Geophysics, Geosystems*, 14, 751–758, <https://doi.org/10.1002/ggge.20071>, 2013.
- Strogatz, S. H.: Nonlinear dynamics and chaos: with applications to physics, biology, chemistry, and engineering, CRC press, 2018.

- Teng, H. and Branstator, G.: Amplification of waveguide teleconnections in the Boreal summer, *Curr. Clim. Change Rep.*, 5, 421–432, <https://doi.org/doi.org/10.1007/s40641-019-00150-x>, 2019.
- 545
- White, R. H., Kornhuber, K., Martius, O., and Wirth, V.: From atmospheric waves to heatwaves: A waveguide perspective for understanding and predicting concurrent, persistent and extreme extratropical weather, *Bull. Amer. Meteor. Soc.*, 103, E923–E935, <https://doi.org/10.1175/BAMS-D-21-0170.1>, 2022.
- Wirth, V.: Waveguidability of idealized midlatitude jets and the limitations of ray tracing theory, *Weather Clim. Dynam.*, 1, 111–125, <https://doi.org/10.5194/wcd-1-111-2020>, 2020.
- 550
- Wirth, V. and Polster, C.: The problem of diagnosing jet waveguidability in the presence of large-amplitude eddies, *J. Atmos. Sci.*, pp. 3137–3151, <https://doi.org/10.1175/JAS-D-20-0292.1>, 2021.
- Wirth, V., Riemer, M., Chang, E. K. M., and Martius, O.: Rossby wave packets on the midlatitude waveguide – A review, *Mon. Wea. Rev.*, 146, 1965–2001, <https://doi.org/10.1175/MWR-D-16-0483.1>, 2018.
- 555
- Yang, G.-Y. and Hoskins, B. J.: Propagation of Rossby waves of nonzero frequency, *J. Atmos. Sci.*, 53, 2365–2378, 1996.